

Available online at www.sciencedirect.com

jmr&t
Journal of Materials Research and Technology
www.jmrt.com.br



Original Article

Effect of the carbon loading on the structural and photocatalytic properties of reduced graphene oxide-TiO₂ nanocomposites prepared by hydrothermal synthesis



Bruno S. Gonçalves^a, Hugo G. Palhares^{a,b}, Tarcizo C.C. de Souza^{b,c},
Vinícius G. de Castro^c, Glaura G. Silva^{c,d}, Bruno C. Silva^e, Klaus Krambrock^e,
Renata B. Soares^b, Vanessa F.C. Lins^b, Manuel Houmard^f, Eduardo H.M. Nunes^{a,*}

^a Departamento de Engenharia Metalúrgica e de Materiais, Universidade Federal de Minas Gerais, Pampulha, CEP: 31270-901, Belo Horizonte, MG, Brazil

^b Departamento de Engenharia Química, Universidade Federal de Minas Gerais, Brazil

^c Centro de Tecnologia em Nanomateriais (CTNano), Rua Professor José Vieira de Mendonça, 1000 - Engenho Nogueira, CEP: 31310-260, Belo Horizonte, MG, Brazil

^d Departamento de Química, Universidade Federal de Minas Gerais, Brazil

^e Departamento de Física, Universidade Federal de Minas Gerais, Brazil

^f Departamento de Engenharia de Materiais e Construção, Brazil

ARTICLE INFO

Article history:

Received 8 March 2019

Accepted 10 October 2019

Available online 11 November 2019

Keywords:

TiO₂

Reduced graphene oxide

Sol-gel process

Structural characterization

Photocatalytic evaluation

ABSTRACT

This work deals with the preparation of reduced graphene oxide (RGO)-TiO₂ composites by a one-step hydrothermal treatment. The effect of the RGO loading on both the structural properties and photocatalytic behavior of RGO-TiO₂ is deeply addressed herein. The hydrothermal treatment promoted the reduction of graphene oxide, crystallization of TiO₂ into anatase, and anchoring of TiO₂ nanoparticles on RGO sheets. It was observed that the prepared anatase particles showed sizes below 10 nm, whereas the RGO sheets displayed thicknesses smaller than 1 nm. The use of RGO at concentrations up to 15 wt% greatly increased the specific surface area of RGO-TiO₂. It was demonstrated that the combination of RGO and TiO₂ gives rise to materials with improved photocatalytic properties and tailored structural properties. The composite with the highest photoactivity was the one containing an RGO loading of 1 wt%; this composite displayed a photocatalytic rate constant about 9.5 times higher than that evaluated for pure TiO₂. This behavior may be related to the stacking of RGO nanosheets when its concentration is above 1 wt%. Moreover, the addition of RGO in excess may prevent the activation of the TiO₂ surface by UV light and also decrease the lifetime of the photogenerated electron-hole pairs. Therefore, it

* Corresponding author.

E-mails: brunosg.eq@gmail.com (B.S. Gonçalves), mhoumard@ufmg.br (M. Houmard), eduardo.nunes@demet.ufmg.br (E.H. Nunes).

<https://doi.org/10.1016/j.jmrt.2019.10.020>

2238-7854/© 2019 The Authors. Published by Elsevier B.V. This is an open access article under the CC BY-NC-ND license (<http://creativecommons.org/licenses/by-nc-nd/4.0/>).

appears that 1 wt% is the optimal loading of RGO to obtain a close interfacial contact between RGO and TiO₂, leading to both an effective activation of TiO₂ by UV radiation and an enhanced charge transfer between RGO and TiO₂.

© 2019 The Authors. Published by Elsevier B.V. This is an open access article under the CC BY-NC-ND license (<http://creativecommons.org/licenses/by-nc-nd/4.0/>).

1. Introduction

Titania (TiO₂) is the naturally occurring oxide of titanium under atmospheric conditions. It mainly shows three polymorphic phases, namely rutile, anatase, and brookite [1]. TiO₂ is commonly employed in several applications, including solar cells [2], self-cleaning surfaces [3,4], and photocatalysis [5,6]. The photocatalytic properties of TiO₂ are ascribed to electron-hole pairs generated by ultraviolet (UV) light. In this process, electrons are promoted from the valence band to the conduction one, creating holes in the former band. The photogenerated holes may diffuse towards the surface, reacting with adsorbed water molecules and giving rise to hydroxyl radicals. Both the photogenerated holes and hydroxyl radicals oxidize organic molecules at the surface of TiO₂. Moreover, the electrons promoted to the conduction band may participate in reduction processes, which typically lead to the production of superoxide radicals (O₂⁻) [7].

Different approaches have been used to improve the photocatalytic behavior of TiO₂. For instance, it has been shown a dramatic increase in the photoactivity of this material when it contains both rutile and anatase [8]. Rutile and anatase exhibit band gaps around 3.03 and 3.20 eV, respectively [9]. It has been reported that this energy difference favors the transference of electron and holes between these two phases, increasing the lifetime of the photogenerated charge carriers and improving the photoactivity of TiO₂ [10]. The doping of TiO₂ has also been widely used for either narrowing its bandgap or introducing energy levels into the forbidden band [11,12]. Carbon nanostructures such as nanotubes (CNT) and reduced graphene oxide (RGO) are also commonly used to obtain TiO₂-based composites with enhanced photocatalytic properties. For instance, Zouzelka et al. [13] observed a significant increase in the degradation rate of 4-chlorophenol when multiwalled CNT-TiO₂ composites were compared to commercial TiO₂ samples. Min et al. [14] noticed a similar behavior for RGO-TiO₂ composites employed in the photocatalytic decolorization of methylene blue (MB). It has been reported that the transference of photogenerated electron and holes between the carbon nanostructure and TiO₂ crystals plays a key role in the photoactivity of the obtained composites [15,16].

In this work, RGO-TiO₂ nanocomposites were prepared by a one-step hydrothermal treatment. In this treatment, RGO sheets and amorphous TiO₂ nanoparticles were initially obtained by the ultrasonic exfoliation of graphite oxide (GrO) and sol-gel process, respectively. Next, hydrothermal treatment was conducted in a Teflon-lined stainless steel autoclave at 180 °C. It was demonstrated that the hydrothermal treatment promoted the reduction of graphene oxide, transformation of amorphous TiO₂ into anatase, and anchoring of TiO₂ nanoparticles on RGO sheets. The obtained

materials were examined by several techniques, including X-ray diffraction (XRD), atomic force microscopy (AFM), N₂ adsorption, Raman spectroscopy, ultraviolet-visible (UV-Vis) spectroscopy, transmission electron microscopy (TEM), electrochemical impedance spectroscopy (EIS), and electron paramagnetic resonance (EPR). Their photocatalytic activity was evaluated by measuring the degradation rate of MB under UV irradiation. Few papers available in the literature correlate the structural properties of RGO-containing composites to their catalytic behavior. The effect of the RGO loading on both the textural properties and photocatalytic behavior of RGO-TiO₂ composites is deeply addressed in this study.

2. Materials and methods

2.1. Syntheses

2.1.1. Graphene oxide (GO) nanosheets

The synthesis of GO nanosheets was based on a procedure described in detail in the Brazilian patent BR 102016005632-2 A2 [17]. Briefly, a solution of 360 mL of sulfuric acid (H₂SO₄ / Synth / 98%) and 15 g of potassium permanganate (KMnO₄ / Neon / 99%) was initially prepared under stirring in an ice bath. 7.5 g of graphite powder (CBG Mining) was then added to this solution. The as-prepared slurry was kept under stirring in a microwave digestion system (Milestone Start D) at 250 W and 70 °C for 10 min. Next, the slurry was dispersed in ice-cooled deionized water, followed by the addition of an aqueous solution containing hydrogen peroxide (35 vol%) to remove the manganese impurities. The slurry was filtered and the remaining solid graphite oxide (GrO) was continuously washed with deionized water until reaching pH 7. GO was subsequently obtained by the ultrasonic exfoliation of GrO in water for 30 min. The as-prepared suspension was centrifuged at 4000 rpm for 20 min and GO was collected as supernatant. The concentration of GO in the obtained aqueous suspension was 5.3 g·L⁻¹.

2.1.2. TiO₂ stock solution

A TiO₂ stock solution was prepared by the sol-gel process [18]. A typical procedure is as follows. A solution of isopropyl alcohol (IPA / Aldrich / 98%) and hydrochloric acid (HCl / Aldrich / 37%) was initially prepared under stirring at room temperature. In another container, titanium tetraisopropoxide (TIPT / Aldrich / 98%), IPA, and deionized Milli-Q water were also mixed. The concentration of TIPT in this solution was kept constant at 0.4 M. After the homogenization of both solutions, they were mixed and aged at room temperature for at least three days. The molar ratio of TIPT: IPA: H₂O in the as-prepared solution was 1: 0.13: 0.82. This solution was then diluted in Milli-Q water to obtain a sol with a TIPT: H₂O molar ratio of 1:

90. At this point, amorphous TiO₂ nanoparticles were present in the sol.

2.1.3. RGO-TiO₂

RGO-TiO₂ composites were obtained by adding the previously-prepared aqueous dispersion of GO into the titania sol. The amount of GO used in this step was varied to prepare samples with different RGO loadings, ranging from 0 to 20 wt%. The as-prepared solutions were stirred at room temperature for homogenization. They were then poured in an autoclave and heat-treated at 180 °C for up to 6 h. This procedure promotes the reduction of GO, crystallization of TiO₂ into anatase, and anchoring of TiO₂ nanoparticles on the RGO sheets [19,20]. Pure TiO₂ nanoparticles were also prepared for comparison purposes.

2.2. Structural characterization and photocatalytic tests

XRD was conducted on a Philips-PANalytical PW1710 diffractometer at a scan speed of 0.06°·s⁻¹ using CuK α as the radiation source (1.54 Å). Raman spectroscopy was performed on a Jobin-Yvon Horiba LabRAM HR 800 apparatus at a step size of 1.1 cm⁻¹ with excitation radiation of 632.82 nm (He-Ne laser). N₂ adsorption was carried out on a Quantachrome Nova 1200e system using samples previously degassed under vacuum at 130 °C for up to 48 h. The specific surface area (SSA) was evaluated by the multipoint BET (Brunauer-Emmett-Teller) method. AFM was conducted on an Asylum Research MFP-3D microscope operating in the tapping mode. It was used a silicon cantilever exhibiting a spring constant of 26 N·m⁻¹ and resonance frequency of 300 kHz. These tests were performed by dripping the aqueous suspension of GO onto a mica substrate. SEM was carried out at an accelerating voltage of 5 kV on an FEI Quanta FEG 3D microscope coupled with an EDS analysis system (EDAX – Pegasus Microanalyser). The samples used in these tests were initially dispersed in acetone, sonicated at room temperature for at least 5 min and dripped onto SEM stubs previously coated with double-sided carbon tape. TEM was carried out with an FEI Tecnai G2-20 SuperTwin microscope at an accelerating voltage of 200 kV. Samples used in these examinations were previously dispersed in absolute ethanol and sonicated for at least 5 min. The as-obtained suspensions were then dripped onto carbon-coated grids. After drying at room temperature, these grids were used in the TEM/SAED tests. The bandgap energy (E_g) of the materials prepared herein was assessed by UV-Vis diffuse reflectance spectroscopy with a Shimadzu UV-2600 apparatus at a resolution of 1 cm⁻¹. The Kubelka-Munk and Tauc methods were applied in these calculations, following the methodology recommended by López and Gómez [21].

EIS was conducted at room temperature with an Autolab PGSTAT 100 N potentiostat and using a NaCl-containing aqueous solution (3.5%). Polished stainless steel substrates were coated with either TiO₂ or RGO-TiO₂ to conduct these tests. The deposition step was performed by dripping water-based solutions containing TiO₂ or RGO-TiO₂ on the substrates, followed by air-drying at 80 °C for about 1 h. A bare stainless steel substrate was also examined for reference purposes. A three-electrode cell was used in EIS: saturated calomel was

employed as the reference electrode, platinum as the counter-electrode, and stainless steel as the working electrode. The surface area evaluated in these experiments was kept constant at about 1 cm². Samples were kept immersed in the NaCl-containing solution for 1 h prior EIS tests for stabilization purposes. EIS was performed at a scan speed of 1 mV·s⁻¹ and within a frequency range between 5 × 10⁻³ and 10⁴ Hz. A potential amplitude of 10 mV was used in these tests. Aiming to explore the underlying mechanisms of the photodegradation of MB by TiO₂-based materials under UV illumination, EPR spectroscopy coupled with spin-trapping was also applied in this study. This method allows identifying and quantifying short-lived free radicals, in particular, reactive oxygen species (ROS). Aqueous solutions of PBN (alpha-phenyl N-tertiary-butyl nitron), DMPO (5,5-dimethyl-pyrroline N-oxide) and TMP (2,2,6,6-tetramethylpiperidine) were used as spin-traps. The initial concentrations of PBN, DMPO, and TPM were 50 mM, 50 mM, and 1 M, respectively. Moreover, sodium oxalate (Na₂C₂O₄) and tiron (C₆H₄Na₂O₈S₂) were used as scavengers for free holes and superoxide radicals, respectively. The concentrations of sodium oxalate and tiron were 20 and 50 mM, respectively. It was prepared aqueous suspensions containing 6 mg of photocatalyst dispersed in distilled water and different spin-traps. The suspensions were illuminated with UVA light (366 nm, 5 W) while they were kept under stirring at room temperature. Aliquots of 30 μL of the supernatant were collected at different times, poured into glass capillaries, and examined by EPR. The tests were performed on an X-band (9.40 GHz) commercial spectrometer (Magnetech MiniScope MS400, Germany) at room temperature. Typical parameters for the measurements were: center field 337 mT, scan width 10 mT, 60 s acquisition time, 100 kHz field modulation, and 0.2 mT modulation amplitude.

The photocatalytic behavior of the samples prepared in this study was evaluated by measuring the degradation rate of MB (Aldrich) under UV irradiation. These tests were performed using a reactor similar to that described elsewhere [22]. This system displays an Osram Dulux 9W/78 UVA lamp covered with a quartz bulb, which avoids the direct contact of the lamp with the tested material. The solution temperature was kept constant at 25 °C due to a cooling system connected to the reactor. The concentration of MB in the prepared solutions was fixed at 10 mg·L⁻¹ and their initial pH was 4.2. The loading of TiO₂ and RGO-TiO₂ in these solutions was kept at 100 mg·L⁻¹. The degradation tests were preceded by adsorption tests in the absence of UV illumination for 60 min. Photolysis and degradation tests using pure TiO₂ were also performed for reference purposes. The concentration of MB in these solutions was assessed as a function of time with a UV-Vis spectrometer (Cole Parmer 1100 RS). To avoid the absorbance interference from suspended particles, the solutions examined by UV-Vis were previously centrifuged at 1700 rpm for up to 10 min for allowing the settlement of particles. Next, the supernatant was filtered with a PVDF filter (Millex® / 0.45 μm) and subsequently transferred to 1.2 mL poly (methyl methacrylate) (PMMA) cuvettes. The samples were then examined taking into account the absorbance assessed at 665 nm. The concentration of total organic carbon (TOC) was evaluated in MB solutions before and after performing the photocatalytic tests. These tests were conducted on a Shimadzu TOC-V CNP ana-

lyzer following recommendations of the Standard Methods for Examination of Water and Wastewater [23]. The solutions used in these examinations were previously subjected to the afore-described centrifuging and filtration steps to remove suspended particles.

3. Results and discussion

Fig. 1 depicts an AFM image obtained after examining a mica substrate coated with the aqueous dispersion of GO. One observes that the GO sheets are well dispersed and exhibit a thickness of about 0.85 nm. Similar thicknesses were obtained in other AFM images taken in this study. Fig. 2a shows XRD patterns of RGO, TiO₂, and RGO-TiO₂. The broad reflections observed for RGO at about 24° and 43° (2θ) were also reported elsewhere [24] and reveal that GO was successfully reduced to RGO during the hydrothermal treatment. According to Pei and Cheng [25], the observation of a broad halo at 24° may indicate the formation of nanosheets showing thicknesses of a few layers, which is in agreement with AFM (Fig. 1). Anatase was the only crystalline phase observed for TiO₂ and RGO-TiO₂. It was already reported that the methodology used in this work for preparing TiO₂ gives rise to anatase samples [20].

Fig. 2b exhibits Raman spectra taken in this study. The features at 154, 400, 515 and 640 cm⁻¹ are respectively due to E_g, B_{1g}, B_{1g} + A_{1g}, and E_g vibration modes of anatase [26]. This result is in line with XRD (Fig. 2a). The broad bands at about 1320 and 1590 cm⁻¹ observed for RGO are associated with the D and G bands of graphene. The D band has been attributed to edge or in-plane sp³ defects, whereas the G one is due to in-plane vibration of ordered sp²-bonded carbon atoms [27]. Two additional features related to 2D and S3 bands of graphene were observed at about 2645 and 2920 cm⁻¹, respectively [28]. It can be noted that the composites exhibited bands associated with both TiO₂ and RGO. All composites displayed similar Raman spectra, but it was observed that the absorption bands ascribed to RGO become more noticeable the larger is its concentration in the composite. The mean ratio between the intensities of the D and G bands for the composites prepared herein was 1.32 ± 0.03. It has been reported that this intensity ratio is strongly related to the presence of structural defects in carbon. The observation of an intensity ratio above 1.00 may indicate the occurrence of fragmentation in sp² domains during the hydrothermal treatment [29].

Fig. 3 shows TEM micrographs of RGO, TiO₂, and RGO-TiO₂. Thin carbon sheets are observed for RGO, whereas nanoparticles showing sizes below 10 nm are noticed for TiO₂. It can be observed that TiO₂ nanoparticles were successfully anchored onto RGO sheets in RGO (20 wt%)-TiO₂. Selected-area electron diffraction (SAED) tests conducted in these images revealed that anatase is the only crystalline phase observed in the examined materials. This finding suggests that the hydrothermal treatment promoted the phase transformation of amorphous TiO₂ into anatase, which is in agreement with XRD (Fig. 2a).

Fig. 4a displays N₂ adsorption isotherms collected in this work. Both TiO₂ and RGO-TiO₂ exhibited a type-IV isotherm, revealing that they show mesoporous structures [30]. A hysteresis loop ascribed to the capillary condensation of N₂ into

mesopores is observed in these curves. On the other hand, no hysteresis loop was noticed for RGO. Fig. 4b shows SSA as a function of the RGO concentration. A nearly linear increase of SSA was observed when the RGO loading was changed from 0 (166 m².g⁻¹) to 0.5 (187 m².g⁻¹), 1 (189 m².g⁻¹), 2.5 (198 m².g⁻¹), 5 (219 m².g⁻¹), 10 (257 m².g⁻¹) or 15 wt% (273 m².g⁻¹). Nonetheless, further additions of RGO (20 wt%) decreased SSA from 273 to 231 m².g⁻¹ (RGO (20 wt%)-TiO₂). Plain RGO displayed an SSA of about 150 m².g⁻¹. It appears that the combination of RGO and TiO₂ may reduce the agglomeration of TiO₂ nanoparticles and RGO nanosheets [31]. This behavior can explain why the composites showed larger SSA than either TiO₂ or RGO. However, the addition of RGO loadings as high as 20 wt% may favor the stacking of RGO sheets, leading to a decrease of SSA. The stacking of RGO layers is clearly observed in Fig. 3.

Fig. 5a depicts the plot of [F(R)hν]^{1/2} as a function of the photon energy (hν, where h is the Planck constant and ν the photon frequency). F(R) is proportional to the so-called extinction coefficient, and it can be expressed by Eq. (1):

$$F(R) = \frac{(1 - R)^2}{2R}, \quad (1)$$

where R is the reflectance assessed by UV-Vis. E_g can be assessed by extrapolating the line tangent to the inflection point of [F(R)hν]^{1/2}, as schematically shown in Fig. 5a. Fig. 5b exhibits E_g as a function of the RGO loading. From Fig. 5b, one observes that the higher the RGO concentration, the smaller E_g is. It is well established that the electrical conductivity of RGO is strongly related to its oxidation level; highly-reduced GO shows no bandgap, leading to high electron mobility [32]. Based on this behavior, it is plausible to expect that E_g should decrease with increasing the RGO loading.

Fig. 6 shows the Nyquist plots obtained by EIS. The semicircle observed in these curves can be associated with the charge transfer at the electrode/electrolyte interface [33]. The deposition of a TiO₂ film on the stainless steel substrate increased the semicircle radius, revealing that the as-prepared sample has a lower electrical conductivity than the bare substrate. On the other hand, the presence of an RGO (1 wt%)-TiO₂ coating on the steel substrate decreased the Nyquist semicircle of the latter, pointing out that the composite displays a higher electrical conductivity. As discussed before, RGO displays high electron mobility, which leads to samples with smaller bandgaps (Fig. 5b) and higher electrical conductivities when compared to pure TiO₂. It has been reported that smaller Nyquist semicircles are ascribed to more effective separation of electron-hole pairs [34]. As a result, it could be suggested that the separation of the charge carriers created during UV illumination is more effective in the RGO-containing samples.

The adsorption and photocatalytic behavior of the TiO₂-based samples fabricated in this work are shown in Fig. 7. As aforementioned, the samples were kept under the dark condition for 60 min before starting the photocatalytic tests. This approach was used for evaluating the adsorption behavior of the tested materials. TiO₂ showed a small adsorption capacity when compared to RGO-TiO₂. Moreover, it can be observed that the larger the RGO loading, the higher the adsorption capacity of the prepared composites is. It has been reported in the literature that graphene-based materials exhibit a high

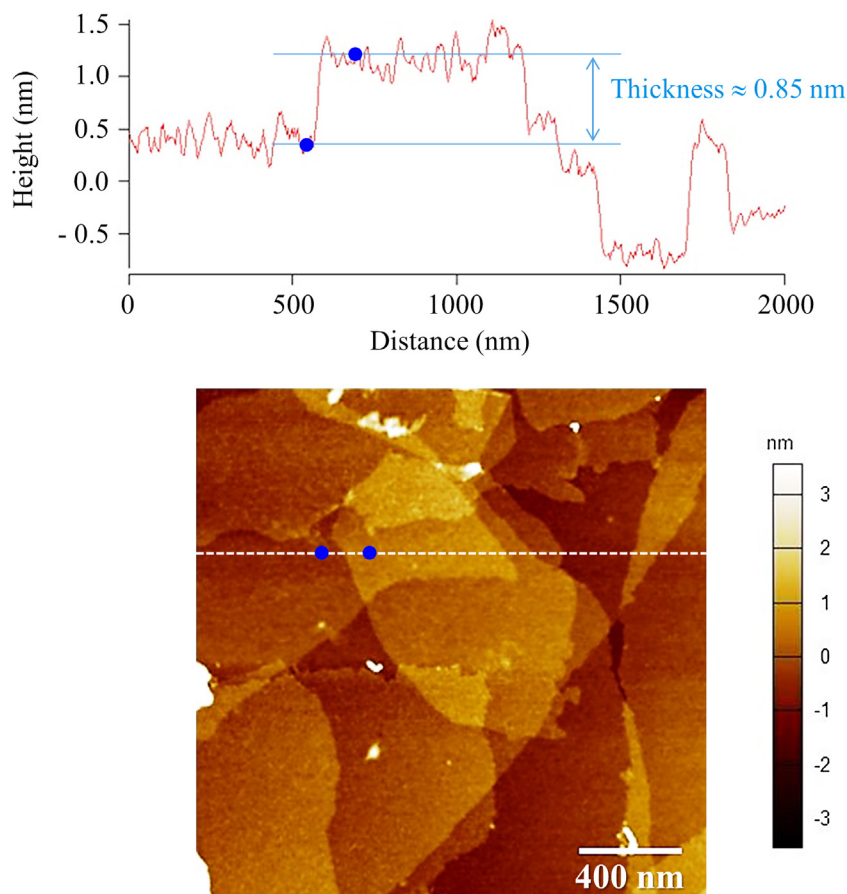


Fig. 1 – AFM image and measured thickness for GO sheets prepared in this work. The height profile was assessed along the dashed line drawn in the AFM image.

adsorption capacity of MB [35,36]. The degradation of MB under UV irradiation (photolysis) was negligible when compared to the degradation level reached when the samples prepared herein were used in the tests. Consequently, the photolysis of MB will not be taken into account in further discussions. The inset of Fig. 7 displays the TOC concentration as a function of time in an MB solution subjected to a photocatalytic test. This test was conducted in the presence of an RGO (1 wt%)-TiO₂ composite. One observes that a decrease of the TOC concentration took place as the photodegradation time increased, revealing that MB experienced degradation during these experiments.

The kinetic model of Langmuir-Hinshelwood (L-H) has been widely used for investigating the photocatalysis of many dyes by TiO₂. This model is expressed by Eq. (2) [37]:

$$r = \frac{dC}{dt} = \frac{kKC}{1 + KC}, \quad (2)$$

where r represents the oxidation rate of the dye ($\text{mg}\cdot\text{L}^{-1}\cdot\text{min}^{-1}$), C the dye concentration ($\text{mg}\cdot\text{L}^{-1}$), t the irradiation time (min), k the reaction rate ($\text{mg}\cdot\text{L}^{-1}\cdot\text{min}^{-1}$) and K the adsorption coefficient ($\text{L}\cdot\text{mg}^{-1}$). For highly diluted

solutions (C_0 within the range of millimolar), Eq. (2) can be simplified to an apparent first-order expression [37,38]:

$$\ln\left(\frac{C}{C_0}\right) = kKt = k_{\text{app}}t, \quad (3)$$

where k_{app} (min^{-1}) is the apparent first-order rate constant. The constant k_{app} can be assessed by plotting $\ln(C/C_0)$ as a function of time.

Fig. 8a and 8b depict, respectively, the plot of $\ln(C/C_0)$ versus t and the values assessed for k_{app} based on the curves shown in Fig. 7. All linear fittings exhibited correlation coefficients (R^2) above 0.99, revealing that the L-H kinetic model can be used for investigating the photocatalytic degradation of MB by TiO₂ and RGO-TiO₂. TiO₂ exhibited a k_{app} around $2.0 \times 10^{-3} \text{ min}^{-1}$, whereas the use of an RGO loading of 1 wt% gave rise to a composite displaying a degradation rate as high as $1.9 \times 10^{-2} \text{ min}^{-1}$. Thus, RGO (1 wt%)-TiO₂ showed a rate constant about 9.5 times higher than that evaluated for TiO₂. At this point, it is worth mentioning that this behavior was also observed when RGO-TiO₂ was obtained using absolute ethanol as the solvent in the sol-gel synthesis of the TiO₂ sol (this finding will be shown in a next work). Further additions of RGO led to materials showing smaller values of k_{app} when compared to RGO (1 wt%)-TiO₂. This behavior may be associated with the stacking of RGO nanosheets when its loading is

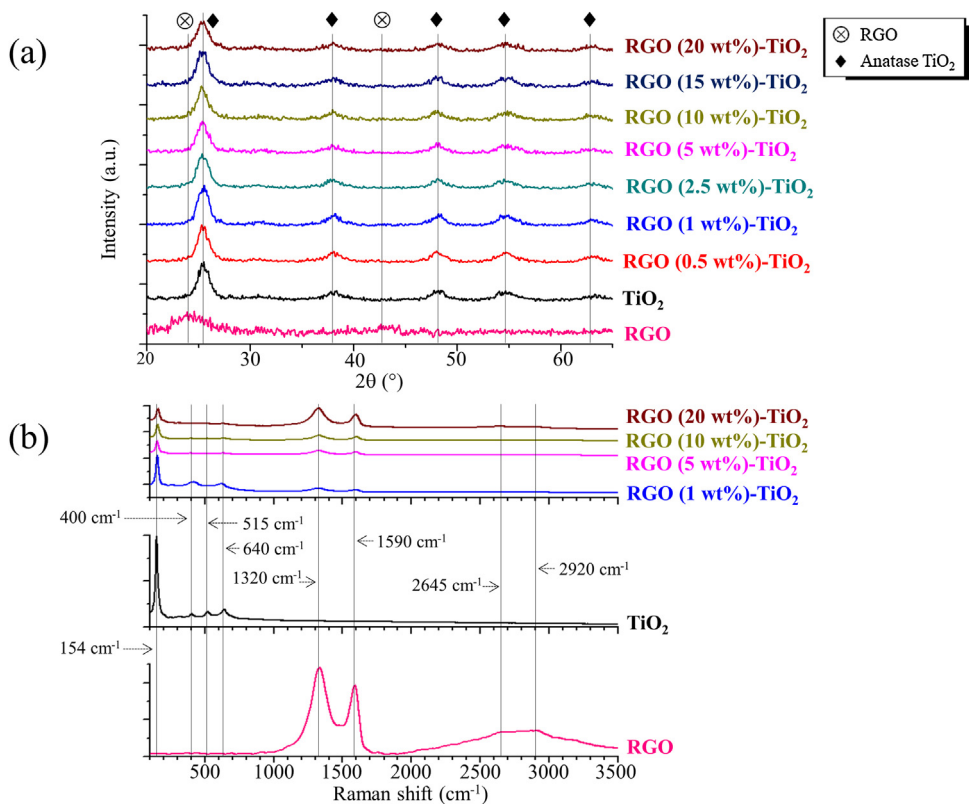


Fig. 2 – (a) XRD patterns of RGO, TiO₂, and RGO-TiO₂ composites. The JCPDS file number 21-1272 was used as a reference for the anatase phase. (b) Raman spectra of RGO, TiO₂, and RGO-TiO₂ composites.

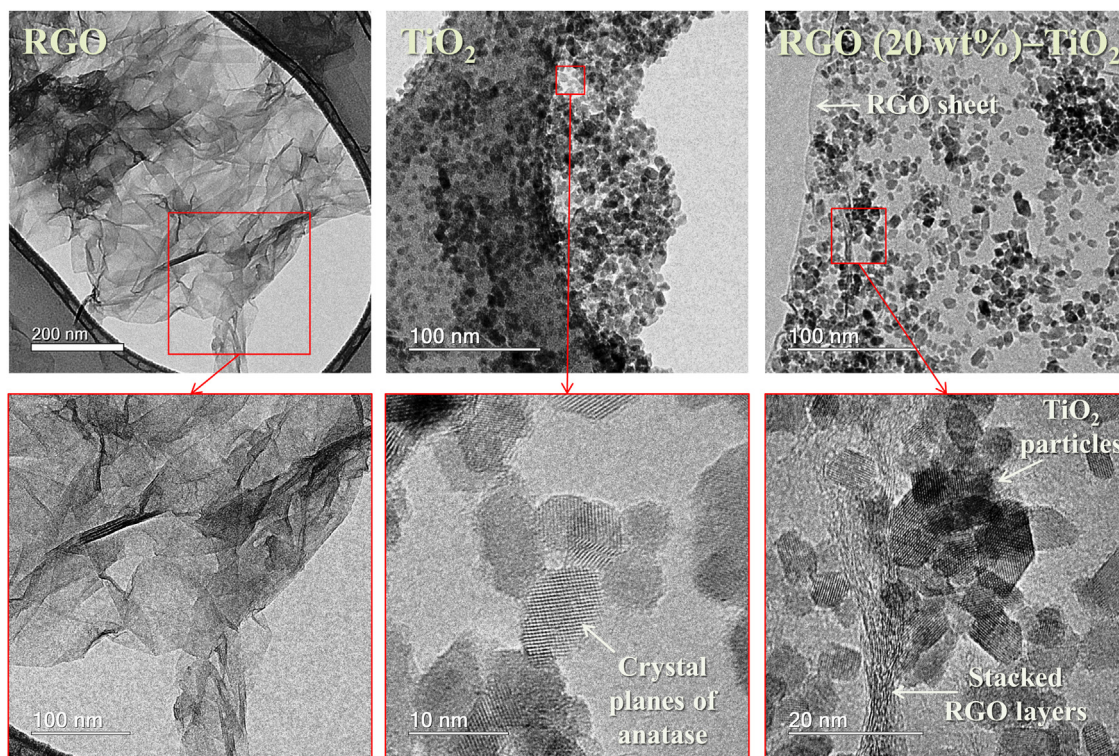


Fig. 3 – TEM micrographs obtained for RGO, TiO₂, and RGO (20 wt%)-TiO₂.

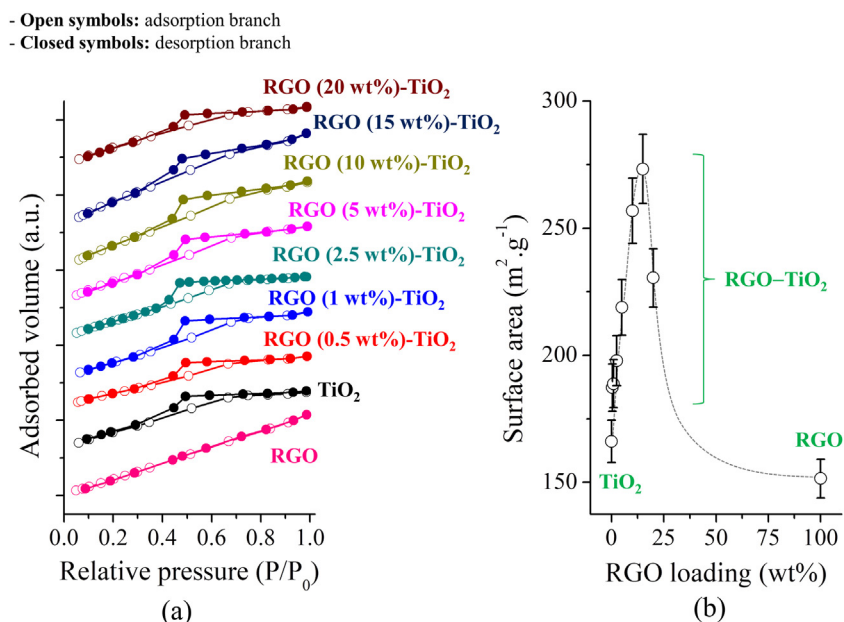


Fig. 4 – (a) N_2 adsorption isotherms and (b) SSA evaluated for TiO_2 and RGO- TiO_2 . The solid lines connecting the data points in Fig. 4b are used as a guide to the eyes only.

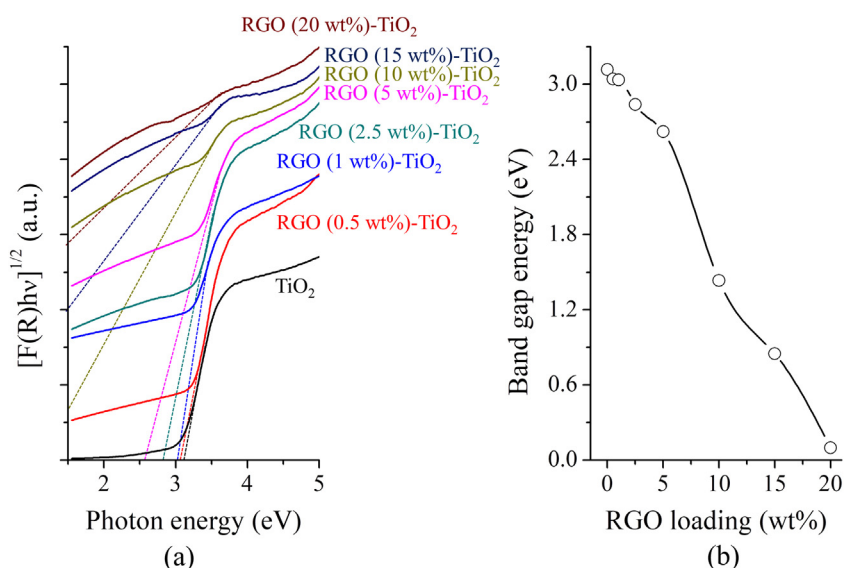


Fig. 5 – (a) $[F(R)h\nu]^{1/2}$ as a function of the photon energy and (b) E_g evaluated for the samples prepared in this work. The solid lines connecting the data points in Fig. 5b are used as a guide to the eyes only.

increased (Fig. 3), which could both partially block the UV radiation and limit the activation of the TiO_2 surface by the light beam [39]. Based on these results, it appears that 1 wt% is the optimal loading of RGO to obtain a close RGO/ TiO_2 interfacial contact, leading to both an effective activation of TiO_2 by UV radiation and an enhanced charge transfer between RGO and TiO_2 . Moreover, composites with RGO loadings above 1 wt% should display a highly negatively charged surface, which could decrease the separation of the photogenerated electron-hole pairs and also result in a fast recombination rate of these charge carriers [40].

In spite of their smaller photoactivity when compared to RGO (1 wt%)- TiO_2 , composites showing RGO loadings rang-

ing from 0.5 to 20 wt% exhibited larger values of k_{app} than TiO_2 (from 2.9×10^{-3} to $4.4 \times 10^{-3} \text{ min}^{-1}$). This finding demonstrates that the use of RGO increased the photoactivity of TiO_2 , which is in agreement with other works [29,41]. As already discussed, it seems that the transference of electron and holes between RGO and TiO_2 increases the lifetime of the photogenerated charge carriers, giving rise to materials with enhanced photocatalytic properties. This synergic effect is strongly related to the high electrical conductivity of RGO, which allows the transference of charge carries between TiO_2 and RGO and increases the lifetime of the photogenerated electron-hole pairs [15,16]. As already discussed, EIS suggested a more effective separation of electron-hole pairs in

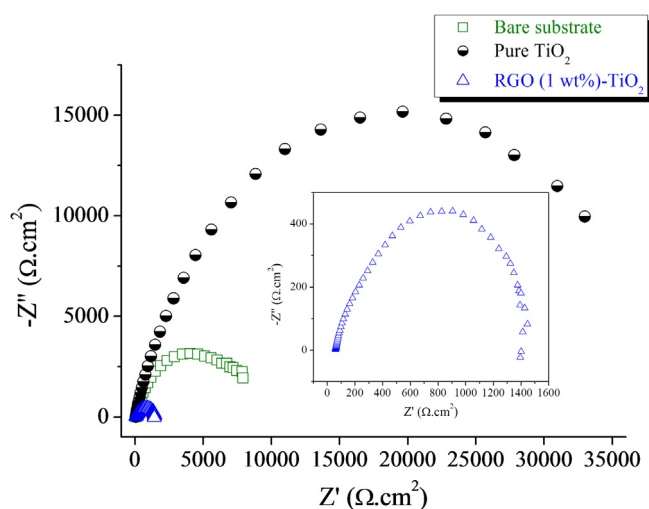
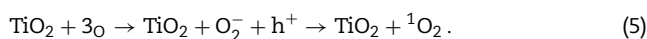
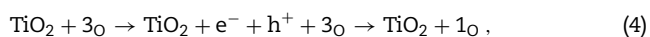


Fig. 6 – Nyquist plots of a stainless steel substrate before and after the deposition of TiO₂ and RGO (1 wt%)-TiO₂ films on it.

RGO-containing samples when compared to pure TiO₂ (Fig. 6), which also contributes to the increase of the lifetime of these charge carriers.

As discussed before, EPR spin-trapping experiments were performed to investigate the mechanisms underlying the photocatalytic properties of the prepared samples under UVA illumination. While the experiments with PBN did not show any photoresponse, i.e., no formation of adducts, the tests performed with DMPO revealed the formation of hydroxyl adducts (not shown). Spin-trapping tests carried out with TMP, a well-known spin-trap for oxygen singlet [42], gave rise to interesting results. Fig. 9a displays a typical three-line hyperfine-split EPR spectrum of TMP adduct after capturing oxygen singlet. Double integration of the derivative-like EPR spectrum leads to the absolute adduct concentration after calibration with a standard sample (1 mM Tempol (1-oxyl-2,2,6,6-tetramethyl-4-hydroxypiperidine) stable radical aqueous solution. Fig. 9b displays the concentration of TMP adducts as a function of the illumination time. Pure TiO₂ and RGO (5 wt%)-TiO₂ showed a nearly linear evolution of TMP adduct formation, i.e., oxygen singlet, but the latter with lower efficiency. RGO (1 wt%)-TiO₂ showed a different behavior, displaying an S-shaped curve for the formation of TMP adduct. In the first 30 min of illumination, it presented a low efficiency in the formation of TMP adduct. However, after this interval, the formation of TMP adduct increased and saturated at an intermediate level when compared to the other two samples.

For photocatalysts based on semiconductor particles, it is expected that the dominant ROS are formed by charge transfer mechanism due to the excitation of electrons (e⁻) from the valence to the conduction band of the semiconductor, leaving holes (h⁺) in the valence band. On the other hand, it is believed that the formation of oxygen singlet is due to an energy transfer mechanism, which excites molecular oxygen ³O₂ to oxygen singlet ¹O₂. The formation of oxygen singlet by semiconductor photocatalysts can be explained in two ways [43]:



An EPR spectrum taken at -173 °C for powdered TiO₂ did not show any relevant paramagnetic species in dark conditions or under UVA illumination. On the other hand, the RGO (1 wt%)-TiO₂ composite exhibited superoxide species when exposed to UVA radiation, which are stable species for long times after switching off the UVA light (not shown). The EPR spectrum of O₂⁻ species showed axial symmetry with g_⊥ = 2.002(2) and g_∥ = 2.018(3), in addition to an asymmetric spectral shape (Dysonian line shape), which indicates the formation of free carriers. These results suggest that for pure TiO₂, light-induced electron and holes effectively recombine, whereas, for RGO (1 wt%)-TiO₂, electrons are capable of producing superoxide species on the surface of the TiO₂ nanoparticles. It is suggestive that holes diffuse away to graphene because other EPR signals due to different paramagnetic species were not observed. Although our experimental data do not allow concluding where the charge recombination occurs, we may suggest that the remaining charge recombination of electron-hole pairs takes place within the TiO₂ particles (where these pairs were produced) or at the interface between TiO₂ and graphene. These results are in agreement with the model recently reported by Martins et al. [44].

Aiming to identify the ROS specimens involved in the formation of TMP adduct, two different suppressors were used, namely sodium oxalate (hole scavenger) and tiron (superoxide radical scavenger) [45,46]. From Fig. 9c, one can notice that tiron can completely remove oxygen singlet, which indicates that superoxide anion is the dominant radical species involved in the photocatalytic process. On the other hand, sodium oxalate also showed some influence on the formation of singlet oxygen, but to a lower extent. If we take into consideration Eqs. (4) and (5), it appears that a great part of the formed oxygen singlet is due to the process represented by Eq. (5).

Superoxide radicals are difficult to directly detect by spin-trapping [47]. PBN does not form adducts with O₂⁻ and DMPO superoxide adducts have limited stability, easily transforming into hydroxyl adducts which present a four-line hyperfine-split EPR spectrum with intensity ratios of 1:3:3:1. Hydroxyl radicals are also captured by PBN. Therefore, our spin-trapping experiments using PBN and DMPO are in-line with the results obtained using TMP spin-trap and tiron superoxide scavenger. Pure TiO₂ showed the most intense signal due to singlet oxygen (Fig. 9b). However, it is less efficient in the photocatalytic degradation of MB. This fact implies that the dominant process for oxygen singlet for this sample is due to the Eq. (4), i.e., the recombination of free electron and holes. On the other hand, the TiO₂ composites based on TiO₂ nanoparticles anchored on RGO sheets result in a more effective separation of electron-hole pairs, reducing the recombination rate of charge carriers and allowing the transfer of electrons to molecular oxygen of the solvent with the subsequent formation of superoxide radicals. It is also worth stressing that holes may also contribute to the photocatalytic process interacting directly with adsorbed substrate molecules, i.e. adsorbed MB molecules on the surface of TiO₂-based composites. These observations explain the higher photoresponse of the RGO (1 wt%)-TiO₂ sample.

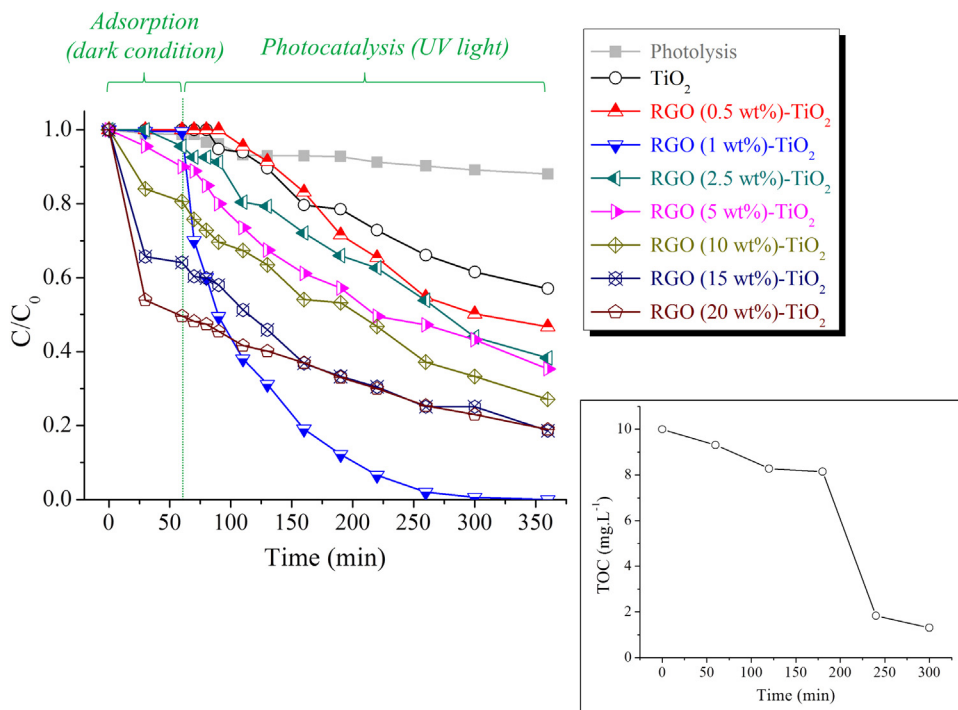


Fig. 7 – Adsorption and photocatalytic behavior of TiO_2 and RGO- TiO_2 . Inset: TOC concentration in an MB-containing solution during a photocatalytic test. The RGO (1wt%)- TiO_2 composite was used in this photocatalytic run. The examined materials were kept under dark conditions for 60 min before their illumination with the UV lamp. The solid lines connecting the data points are used as a guide to the eyes only.

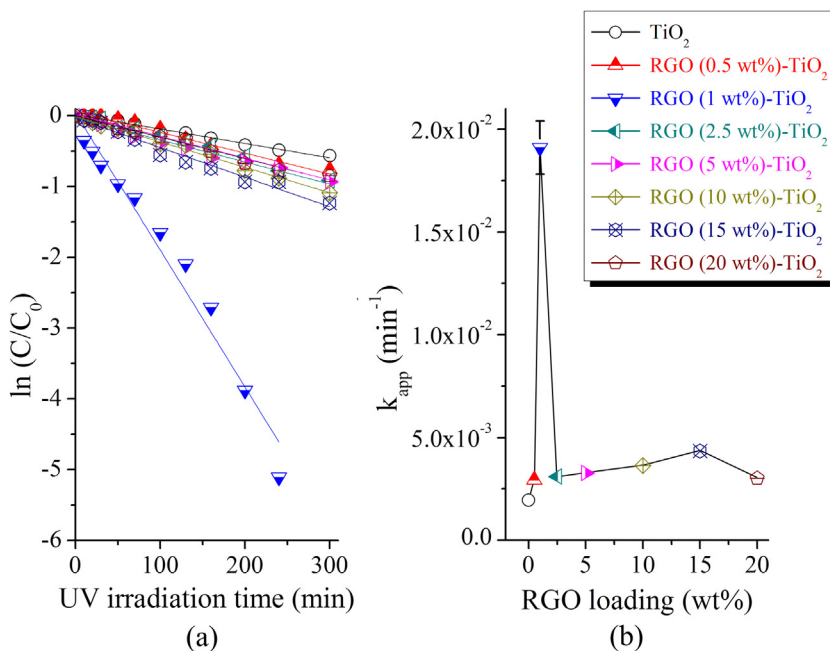


Fig. 8 – (a) $\ln(C/C_0)$ as a function of time and (b) k_{app} for different samples. The solid lines connecting the data points in Fig. 8b are used as a guide to the eyes only.

The reason why the photodegradation of MB is decreased for higher loadings with RGO, i.e. RGO (5 wt%)- TiO_2 , is probably related to the fact that the UVA light cannot efficiently activate the TiO_2 particles due to the strong absorption of light by RGO.

In this study, a one-step simple method is suggested for obtaining RGO- TiO_2 composites from RGO and amorphous TiO_2 suspensions. No heat-treatment at temperatures above $180^\circ C$ was needed for preparing these materials, which represents an important advantage in terms of both energy

Table 1 – Comparison between this work and other ones already published. ND*: not defined.

TiO ₂ starting material	Titanium precursor	GO loading (wt%)	Preparation method of the titania/graphene composite	Radiation	Illumination time (min)	Catalyst concentration (mg.L ⁻¹)	Most photoactive sample	Specific surface area (m ² .g ⁻¹)	Reference
Sol-gel TiO ₂	TIPT	0-20	Hydrothermal treatment	UV-9 W	300	100	RGO (1 wt%)-TiO ₂	189	This work
Commercial aerioxide [®] TiO ₂ P90	–	5-20	Hydrothermal treatment	UV-450 W	60	200	RGO (10 wt%)-TiO ₂	ND*	Perera et al. [39]
Commercial aerioxide [®] TiO ₂ P25	–	1	Hydrothermal treatment	UV-100 W	65	750	RGO (1 wt%)-TiO ₂	51	Zhang et al. [19]
TiO ₂	(NH ₄) ₂ TiF ₆	ND*	Heat-treatment	UV-20 W	9	500	GO-TiO ₂	80	Jiang et al. [28]
Commercial aerioxide [®] TiO ₂ P25	–	1-10	Drying	Vis-150 W	120	1000	TiO ₂	50	Szabó et al. [48]
Sol-gel TiO ₂	TiC ₁₆ H ₃₆ O ₄	1-10	Heat-treatment	UV-500 W	120	500	RGO (5 wt%)-TiO ₂	24	Zhang et al. [49]
Sol-gel TiO ₂	Ti(OC ₄ H ₉) ₄	0-5	Hydrothermal treatment	UV-300 W	40	625	RGO (1 wt%)-TiO ₂	76	Xiang et al. [50]
Sol-gel TiO ₂	TIPT	10-50	Microwave-assisted treatment	UV-8 W	90	1000	1 RGO - 3 TiO ₂	109	Nguyen and Shim [51]
Sol-gel TiO ₂	TIPT	5-15	Hydrothermal treatment	UV-300 W	50	167	RGO (15 wt%)-TiO ₂	98	Wu et al. [52]
Sol-gel TiO ₂	Ti(SO ₄) ₂	5-20	Hydrothermal treatment	UV-250 W	30	500	RGO (20 wt%)-TiO ₂	ND*	Liang et al. [29]
Sol-gel TiO ₂	TiC ₁₆ H ₃₆ O ₄	5-20	Hydrothermal treatment	UV+Vis 150 W	180	1000	GO (30 mg)-TiO ₂	ND*	Zhou et al. [53]
Sol-gel TiO ₂	Ti(SO ₄) ₂	1-500	Heat-treatment	Vis-8 W	2400	ND*	GO - TiO ₂ (100 mg)	168	Štengl et al. [54]
Sol-gel TiO ₂	TiC ₁₆ H ₃₆ O ₄	ND*	Heat-treatment	Sunlight	90	480	RGO - TiO ₂	83	Rezaei and Salem [55]

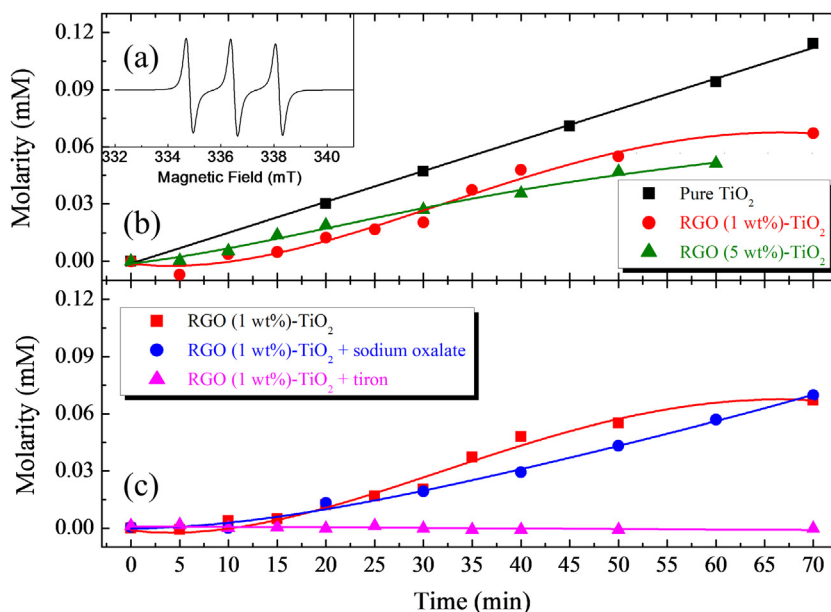


Fig. 9 – EPR spin-trapping experiments conducted with TMP in aqueous solutions containing different TiO₂-based photocatalysts. (a) inset: standard EPR spectrum of TMP adduct; (b) adduct concentrations at different illumination times for pure TiO₂, RGO (1 wt%)-TiO₂, and RGO (5 wt%)-TiO₂; (c) same experiments performed for RGO (1 wt%)-TiO₂ using different scavengers.

and time-saving. It was also demonstrated that the use of an RGO loading as small as 1 wt% was sufficient to prepare nanocomposites with improved photocatalytic properties. The structural properties and photocatalytic behavior of the prepared composites were tailored by changing the RGO loading. Table 1 provides a comparison between this work and other ones already published. The reader is encouraged to refer the original papers to obtain additional details concerning the experimental conditions followed in these studies. As different titanium sources and fabrication methods are used in these works, the prepared materials display distinct photocatalytic performances. It can be observed that the concentration of catalyst in the photocatalytic tests conducted in this work is significantly below those reported in Table 1. One could expect that a lower concentration of catalysts should decrease the adsorption kinetics and consequently the photoactivity of the samples prepared herein. Moreover, the UV lamp used in this study displays a lower power than those used in several works. Nonetheless, the samples fabricated in this study exhibited a high photoactivity regardless of the adverse testing conditions used herein. This behavior reveals the promising performance of these materials, suggesting that they could be used in environmental photocatalytic applications such as the treatment of wastewaters. Besides, it is worth highlighting the large SSA displayed by the samples prepared in this study, which can represent an important advantage in many applications.

4. Conclusions

Reduced graphene oxide (RGO)-TiO₂ composites were successfully prepared in this work. TiO₂ anatase nanoparticles

showing sizes below 10 nm were initially fabricated by the sol-gel process and hydrothermal treatment. The as-obtained suspension was then mixed with a previously prepared graphene oxide (GO) aqueous suspension and hydrothermally treated at 180 °C for 6 h. The hydrothermal treatment of the GO-TiO₂ solution at 180 °C for 6 h in a stainless steel autoclave promoted both the reduction of GO and anchoring of TiO₂ nanoparticles on RGO nanosheets. Anatase was the unique crystalline phase observed in the obtained composite, also revealing that the hydrothermal treatment promoted the crystallization of TiO₂. It was observed that the RGO loading shows a great effect on both the structural properties and photocatalytic behavior of RGO-TiO₂ composites. For instance, the use of RGO at a concentration below 20 wt% greatly increased the specific surface area of the composites. However, the composite with the highest photoactivity was the one showing an RGO loading of 1 wt%. This behavior is probably due to the stacking of RGO nanosheets when its concentration is above 1 wt%. Therefore, it appears that 1 wt% is the optimal loading of RGO to obtain a close RGO/TiO₂ interfacial contact, leading to both an effective activation of TiO₂ by UV radiation and an enhanced charge transfer between RGO and TiO₂. It was evidenced by EPR and EIS spectroscopies a more effective separation of the photogenerated charge carriers in the RGO (1 wt%)-TiO₂ composite, which supports its high photoactivity.

Acknowledgments

The authors thank the financial support from PRPq-UFMG (05/2016), FAPEMIG (APQ-00792-17/red-00102-16), CNPq (305013/2017-3 and 301423/2018) and CAPES (PROEX). UFMG-Microscopy Center is acknowledged for the support provided

in AFM and TEM/SAED. INCT-Acqua (Cláudia Caldeira, Ilda Batista, and Maria Dantas), LEPCom (prof. Rodrigo Oréfice) and Biofuels Laboratory DEMEC-UFMG (prof. Adriana França and Leandro Soares) are kindly acknowledged for the support given to this study.

REFERENCES

- [1] Hanaor DAH, Sorrell CC. Review of the anatase to rutile phase transformation. *J Mater Sci* 2011;46:855–74, <http://dx.doi.org/10.1007/s10853-010-5113-0>.
- [2] Esparza D, Zarazúa I, López-Luke T, Cerdán-Pasarán A, Sánchez-Solís A, Torres-Castro A, et al. Effect of different sensitization technique on the photoconversion efficiency of CdS quantum dot and CdSe quantum rod sensitized TiO₂ solar cells. *J Phys Chem C* 2015;119:13394–403, <http://dx.doi.org/10.1021/acs.jpcc.5b01525>.
- [3] Houmard M, Riassetto D, Roussel F, Bourgeois A, Berthomé G, Joud JC, et al. Enhanced persistence of natural super-hydrophilicity in TiO₂-SiO₂ composite thin films deposited via a sol-gel route. *Surf Sci* 2008;602:3364–74, <http://dx.doi.org/10.1016/j.susc.2008.09.016>.
- [4] Houmard M, Berthomé G, Joud JC, Langlet M. Enhanced cleanability of super-hydrophilic TiO₂-SiO₂ composite surfaces prepared via a sol-gel route. *Surf Sci* 2011;605:456–62, <http://dx.doi.org/10.1016/j.susc.2010.11.017>.
- [5] Cai Q, Hu J. Decomposition of sulfamethoxazole and trimethoprim by continuous UVA/LED/TiO₂ photocatalysis: decomposition pathways, residual antibacterial activity and toxicity. *J Hazard Mater* 2017;323:527–36, <http://dx.doi.org/10.1016/j.jhazmat.2016.06.006>.
- [6] Farner Budarz J, Turolla A, Piasecki AF, Bottero J-Y, Antonelli M, Wiesner MR. Influence of aqueous inorganic anions on the reactivity of nanoparticles in TiO₂ photocatalysis. *Langmuir* 2017;33:2770–9, <http://dx.doi.org/10.1021/acs.langmuir.6b04116>.
- [7] Nakata K, Fujishima A. TiO₂ photocatalysis: design and applications. *J Photochem Photobiol C Photochem Rev* 2012;13:169–89, <http://dx.doi.org/10.1016/j.jphotochemrev.2012.06.001>.
- [8] Ohno T, Tokieda K, Higashida S, Matsumura M. Synergism between rutile and anatase TiO₂ particles in photocatalytic oxidation of naphthalene. *Appl Catal A Gen* 2003;244:383–91.
- [9] Tang H, Prasad K, Sanjinès R, Schmid PE, Lévy F. Electrical and optical properties of TiO₂ anatase thin films. *J Appl Phys* 1994;75:2042–7, <http://dx.doi.org/10.1063/1.356306>.
- [10] Scanlon DO, Dunnill CW, Buckeridge J, Shevlin SA, Logsdail AJ, Woodley SM, et al. Band alignment of rutile and anatase TiO₂. *Nat Mater* 2013;12:798–801, <http://dx.doi.org/10.1038/nmat3697>.
- [11] Khraisheh M, Wu L, Al-Muhtaseb AH, Al-Ghouthi MA. Photocatalytic disinfection of Escherichia coli using TiO₂ P25 and Cu-doped TiO₂. *J Ind Eng Chem* 2015;28:369–76, <http://dx.doi.org/10.1016/j.jiec.2015.02.023>.
- [12] Saqib NU, Adnan R, Shah I. A mini-review on rare earth metal-doped TiO₂ for photocatalytic remediation of wastewater. *Environ Sci Pollut Res* 2016;23:15941–51, <http://dx.doi.org/10.1007/s11356-016-6984-7>.
- [13] Zouzelka R, Kusumawati Y, Remzova M, Rathousky J, Pauport T. Photocatalytic activity of porous multiwalled carbon nanotube-TiO₂ composite layers for pollutant degradation. *J Hazard Mater* 2016;317:52–9, <http://dx.doi.org/10.1016/j.jhazmat.2016.05.056>.
- [14] Min YL, Zhang K, Zhao W, Zheng FC, Chen YC, Zhang YG. Enhanced chemical interaction between TiO₂ and graphene oxide for photocatalytic decolorization of methylene blue. *Chem Eng J* 2012;193–194:203–10, <http://dx.doi.org/10.1016/j.cej.2012.04.047>.
- [15] Hoffmann MR, Martin S, Choi W, Bahnemann DW. Environmental applications of semiconductor photocatalysis. *Chem Rev* 1995;95:69–96, <http://dx.doi.org/10.1021/cr00033a004>.
- [16] Wang W, Serp P, Kalck P, Faria JL. Visible light photodegradation of phenol on MWNT-TiO₂ composite catalysts prepared by a modified sol-gel method. *J Mol Catal A Chem* 2005;235:194–9, <http://dx.doi.org/10.1016/j.molcata.2005.02.027>.
- [17] Castro VG, Neves JC, Pereira NM, Assis ALS, Montoro LA, Silva GG. Process for obtaining graphite oxide and graphene oxide: products and uses. *BR 102016005632-2 A2*; 2017.
- [18] Langlet M, Kim A, Audier M, Guillard C, Herrmann JM. Liquid phase processing and thin film deposition of titania nanocrystallites for photocatalytic applications on thermally sensitive substrates. *J Mater Sci* 2003;38:3945–53, <http://dx.doi.org/10.1023/A:1026150213468>.
- [19] Zhang H, Lv X, Li Y, Wang Y, Li J. P25-graphene composite as a high performance photocatalyst. *ACS Nano* 2009;4:380–6, <http://dx.doi.org/10.1021/nn901221k>.
- [20] Resende SF, Nunes EHM, Houmard M, Vasconcelos WL. Simple sol-gel process to obtain silica-coated anatase particles with enhanced TiO₂-SiO₂ interfacial area. *J Colloid Interface Sci* 2014;433:211–7, <http://dx.doi.org/10.1016/j.jcis.2014.06.033>.
- [21] López R, Gómez R. Band-gap energy estimation from diffuse reflectance measurements on sol-gel and commercial TiO₂: a comparative study. *J Solgel Sci Technol* 2012;61:1–7, <http://dx.doi.org/10.1007/s10971-011-2582-9>.
- [22] Starling MCV, Castro LAS, Marcelino RBP, Leão MMD, Amorim CC. Optimized treatment conditions for textile wastewater reuse using photocatalytic processes under UV and visible light sources. *Environ Sci Pollut Res* 2016;1–11, <http://dx.doi.org/10.1007/s11356-016-6157-8>.
- [23] APHA, AWWA, WEF. *Standard methods for examination of water and wastewater*; 2012.
- [24] Khan M, Al-Marri AH, Khan M, Shaik MR, Mohri N, Adil SF, et al. Green approach for the effective reduction of graphene oxide using *Salvadora persica* L. Root (Miswak) extract. *Nanoscale Res Lett* 2015;10:1–9, <http://dx.doi.org/10.1186/s11671-015-0987-z>.
- [25] Pei S, Cheng HM. The reduction of graphene oxide. *Carbon N Y* 2012;50:3210–28, <http://dx.doi.org/10.1016/j.carbon.2011.11.010>.
- [26] Song P, Zhang XY, Sun MX, Cui XL, Lin YH. Graphene oxide modified TiO₂ nanotube arrays: enhanced visible light photoelectrochemical properties. *Nanoscale* 2012;4:1800–4, <http://dx.doi.org/10.1039/c2nr11938b>.
- [27] Zhang Y, Zhang N, Tang ZR, Xu YJ. Improving the photocatalytic performance of graphene-TiO₂ nanocomposites via a combined strategy of decreasing defects of graphene and increasing interfacial contact. *Phys Chem Chem Phys* 2012;14:9167–75, <http://dx.doi.org/10.1039/c2cp41318c>.
- [28] Jiang G, Lin Z, Chen C, Zhu L, Chang Q, Wang N, et al. TiO₂ nanoparticles assembled on graphene oxide nanosheets with high photocatalytic activity for removal of pollutants. *Carbon N Y* 2011;49:2693–701, <http://dx.doi.org/10.1016/j.carbon.2011.02.059>.
- [29] Liang D, Cui C, Hub H, Wang Y, Xu S, Ying B, et al. One-step hydrothermal synthesis of anatase TiO₂/reduced graphene oxide nanocomposites with enhanced photocatalytic activity. *J Alloys Compd* 2014;582:236–40, <http://dx.doi.org/10.1016/j.jallcom.2013.08.062>.
- [30] Sing KSW. Reporting physisorption data for gas/solid systems with special reference to the determination of

- surface area and porosity. *Pure Appl Chem* 1982;54:2201-18, <http://dx.doi.org/10.1351/pac198557040603>.
- [31] Tancredi P, Moscoso Londoño O, Rivas Rojas PC, Knobel M, Socolovsky LM. Step-by-step synthesis of iron-oxide nanoparticles attached to graphene oxide: a study on the composite properties and architecture. *Mater Res Bull* 2018;107:255-63, <http://dx.doi.org/10.1016/j.materresbull.2018.08.003>.
- [32] Lian KY, Ji YF, Li XF, Jin MX, Ding DJ, Luo Y. Big bandgap in highly reduced graphene oxides. *J Phys Chem C* 2013;117:6049-54, <http://dx.doi.org/10.1021/jp3118067>.
- [33] Bu Y, Chen Z, Li W, Hou B. Highly efficient photocatalytic performance of graphene-ZnO quasi-shell-core composite material. *ACS Appl Mater Interfaces* 2013;5:12361-8, <http://dx.doi.org/10.1021/am403149g>.
- [34] Shao P, Ren Z, Tian J, Gao S, Luo X, Shi W, et al. Silica hydrogel-mediated dissolution-recrystallization strategy for synthesis of ultrathin alpha-Fe₂O₃ nanosheets with highly exposed (110) facets: a superior photocatalyst for degradation of bisphenol S. *Chem Eng J* 2017;323:64-73, <http://dx.doi.org/10.1016/j.cej.2017.04.069>.
- [35] Wang Y, He Y, Lai Q, Fan M. Review of the progress in preparing nano TiO₂: an important environmental engineering material. *J Environ Sci (China)* 2014;26:2139-77, <http://dx.doi.org/10.1016/j.jes.2014.09.023>.
- [36] Chen L, Li Y, Du Q, Wang Z, Xia Y, Yedinak E, et al. High performance agar/graphene oxide composite aerogel for methylene blue removal. *Carbohydr Polym* 2017;155:345-53, <http://dx.doi.org/10.1016/j.carbpol.2016.08.047>.
- [37] Konstantinou IK, Albanis TA. TiO₂-assisted photocatalytic degradation of azo dyes in aqueous solution: Kinetic and mechanistic investigations: a review. *Appl Catal B Environ* 2004;49:1-14, <http://dx.doi.org/10.1016/j.apcatb.2003.11.010>.
- [38] Houas A, Lachheb H, Ksibi M, Elaloui E, Guillard C, Herrmann JM. Photocatalytic degradation pathway of methylene blue in water. *Appl Catal B Environ* 2001;31:145-57, [http://dx.doi.org/10.1016/S0926-3373\(00\)00276-9](http://dx.doi.org/10.1016/S0926-3373(00)00276-9).
- [39] Perera SD, Mariano RG, Vu K, Nour N, Seitz O, Chabal Y, et al. Hydrothermal synthesis of graphene-TiO₂ nanotube composites with enhanced photocatalytic activity. *ACS Catal* 2012;2:949-56, <http://dx.doi.org/10.1021/cs200621c>.
- [40] Xu F, Na P. String and ball-like TiO₂/rGO Composites with high photo-catalysis degradation capability for methylene blue. *Trans Tianjin Univ* 2018;24:272-81, <http://dx.doi.org/10.1007/s12209-018-0119-9>.
- [41] Trapalis A, Todorova N, Giannakopoulou T, Boukos N, Speliotis T, Dimotikali D, et al. TiO₂/graphene composite photocatalysts for NOx removal: a comparison of surfactant-stabilized graphene and reduced graphene oxide. *Appl Catal B Environ* 2016;180:637-47, <http://dx.doi.org/10.1016/j.apcatb.2015.07.009>.
- [42] Brezová V, Gabčová S, Dvoranová D, Staško A. Reactive oxygen species produced upon photoexcitation of sunscreens containing titanium dioxide (an EPR study). *J Photochem Photobiol B, Biol* 2005;79:121-34, <http://dx.doi.org/10.1016/j.jphotobiol.2004.12.006>.
- [43] Konaka R, Kasahara E, Dunlap WC, Yamamoto Y, Chien KC, Inoue M. Irradiation of titanium dioxide generates both singlet oxygen and superoxide anion. *Free Radic Biol Med* 1999;27:294-300, [http://dx.doi.org/10.1016/S0891-5849\(99\)00050-7](http://dx.doi.org/10.1016/S0891-5849(99)00050-7).
- [44] Martins PM, Ferreira CG, Silva AR, Magalhães B, Alves MM, Pereira L, et al. TiO₂/graphene and TiO₂/graphene oxide nanocomposites for photocatalytic applications: a computer modeling and experimental study. *Compos Part B Eng* 2018;145:39-46, <http://dx.doi.org/10.1016/j.compositesb.2018.03.015>.
- [45] Byrne JA, Eggs BR. Photoelectrochemistry of oxalate on participate TiO₂ electrodes. *J Electroanal Chem (Lausanne)* 1998;457:61-72, [http://dx.doi.org/10.1016/S0022-0728\(98\)00304-0](http://dx.doi.org/10.1016/S0022-0728(98)00304-0).
- [46] Taiwo FA. Mechanism of tiron as scavenger of superoxide ions and free electrons. *Spectroscopy* 2008;22:491-8, <http://dx.doi.org/10.1023/SPE-2008-0362>.
- [47] Brustolon M, Giamello E. Electron paramagnetic resonance: a practitioner's toolkit; 2008, <http://dx.doi.org/10.1002/9780470432235>.
- [48] Szabó T, Veres Á, Cho E, Khim J, Varga N, Dékány I. Photocatalyst separation from aqueous dispersion using graphene oxide/TiO₂ nanocomposites. *Colloids Surfaces A Physicochem Eng Asp* 2013;433:230-9, <http://dx.doi.org/10.1016/j.colsurfa.2013.04.063>.
- [49] Zhang X, Li H, Cui X, Lin Y. Graphene/TiO₂ nanocomposites: synthesis, characterization and application in hydrogen evolution from water photocatalytic splitting. *J Mater Chem* 2010;20:2801-6, <http://dx.doi.org/10.1039/b917240h>.
- [50] Xiang Q, Yu J, Jaroniec M. Enhanced photocatalytic H₂-production activity of graphene-modified titania nanosheets. *Nanoscale* 2011;3:3670-8, <http://dx.doi.org/10.1039/c1nr10610d>.
- [51] Nguyen VH, Shim JJ. Ionic liquid mediated synthesis of graphene-TiO₂ hybrid and its photocatalytic activity. *Mater Sci Eng B Solid-State Mater Adv Technol* 2014;180:38-45, <http://dx.doi.org/10.1016/j.mseb.2013.10.011>.
- [52] Wu H, Fan J, Liu E, Hu X, Ma Y, Fan X, et al. Facile hydrothermal synthesis of TiO₂ nanospindles-reduced graphene oxide composite with an enhanced photocatalytic activity. *J Alloys Compd* 2015;623:298-303, <http://dx.doi.org/10.1016/j.jallcom.2014.10.153>.
- [53] Zhou K, Zhu Y, Yang X, Jiang X, Li C. Preparation of graphene-TiO₂ composites with enhanced photocatalytic activity. *New J Chem* 2011;35:353, <http://dx.doi.org/10.1039/c0nj00623h>.
- [54] Štengl V, Bakardjieva S, Grygar TM, Bludská J, Kormunda M. TiO₂-graphene oxide nanocomposite as advanced photocatalytic materials. *Chem Cent J* 2013;7:41, <http://dx.doi.org/10.1186/1752-153X-7-41>.
- [55] Rezaei M, Salem S. Photocatalytic activity enhancement of anatase-graphene nanocomposite for methylene removal: degradation and kinetics. *Spectrochim Acta - Part A Mol Biomol Spectrosc* 2016;167:41-9, <http://dx.doi.org/10.1016/j.saa.2016.04.075>.